Electronic Supplementary Material (ESI) for Journal of Materials Chemistry C.

Electronic Supporting information

4D Printing with Spin-Crossover Polymer Composites

Mario Piedrahita-Bello,[a,b] José Elias Angulo Cervera,[a,b] Rémi Courson,[b] Gábor Molnár,[a] Laurent Malaquin,[b] Christophe Thibault,[b] Bertrand Tondu,[b] Lionel Salmon,[*,a] Azzedine Bousseksou[*,a]

[a.] Laboratoire de Chimie de Coordination, CNRS UPR 8241, 205 route de Narbonne, F–31077 Toulouse, France. E-mail: lionel.salmon@lcc-toulouse.fr, azzedine.bousseksou@lcc-toulouse.fr

[b.] Laboratoire d'Analyse et d'Architecture des Systèmes, CNRS UPR 8001, 7 avenue du Colonel Roche, F–31400 Toulouse, France.

Methods

Synthesis of the spin crossover complex

All the chemicals and solvents were obtained from Sigma Aldrich and used without any further purification. The spin crossover complex $[Fe(NH_2trz)_3]SO_4$ was prepared using the following procedure: a solution of 6 g of $FeSO_4 \cdot 7H_2O$ (21.6 mmol) in 12 ml of H_2O was added to 5.46 g of 1,2,4-4-NH_2-triazole (65 mmol) in 12 mL of H_2O. The resulting pink solution was stirred during 36 hours and the formed pink precipitate was purified by three successive ethanol washing/centrifugation cycles (yield=81%). Elemental analyses calculated for $[Fe(NH_2trz)_3]SO_4 \cdot 1H_2O$ ($C_6H_{14}N_{12}SO_5Fe$): C, 17.07; H, 3.32; N, 39.82%, found: C, 17.12; H, 2.60; N, 39.78%

3D printing

All the reported designs have been fabricated using a commercial DS-3000 photosensitive polymer (DWS). The spin crossover complex (up to 20 wt%) was mixed and homogenised with the DS-3000 resin during 30 minutes using a Fisherbrand 150 handheld homogenizer. The DWS 29J+ 3D fabrication setup (figure 1) is composed of a bottom part that includes all the optical components. A Solid State BluEdge® BE-1800AHR laser diode is used for the single-photon photopolymerization (emission wavelength: 405 nm, beam diameter: 20 μm). The laser and the optical elements are fixed and galvanometric mirrors move the laser beam along the x and y directions with a maximum writing speed of ca. 6400 mm/s. The second part of the setup is composed of a tank and a sample holder, mounted on a z-axis moving stage, which can ensure a minimum layer thickness of 10 μm and a maximum object height of 10 cm. The volume of the tank is 30 (x) × 25 (y) × 2 (z) cm^3, being able to contain half a litre of photoresist. The maximum object volume, which is printed upside down is of 15 (x) × 15 (y) × 10 (z) cm^3. Between two printed layers a TTT system (Tank Translation Technology) moves the tank

during the printing process to avoid damage of the same area and thus increase its lifetime. The printing process is performed as follows: first the STL (Standard Tessellation Language) file is generated with a CAO 3D software and then processed by the Nauta® software (DWS). The file is then controlled and positioned onto the virtual build table. Pillar supports can be added to facilitate the fabrication of the selected design. Then a Fictor® file is created and loaded into Fictor® software, which cuts the original design into horizontal slices (layers). It is possible to control a maximum of five different regions in z, where the slice, the hatching (gap between two laser trajectories in x, y) and the writing speed can be adapted to the required resolution. For the first layer, the sample holder is moved along the z axis at a distance h0 = 30 to 50 μm from the tank surface depending on the sensitivity of the photoresist. The first layer of the model is exposed according to the laser trajectory defined by the hatching and the writing speed. Once the first layer is exposed, the stage is moved up to a position h0+h where h defines the layer thickness. This procedure is repeated sequentially for the whole sliced design. All the structures produced in this work were obtained using a raster scan filling procedure.

Sample characterization

SEM images were acquired using a JEOL JSM 7800F Prime instrument operated at 5 kV. Samples for SEM were prepared by breaking the film and the cross section was metalized with Pt. Variable-temperature optical reflectivity data were acquired with a MOTIC SMZ-168 stereomicroscope equipped with MOTICAM 1000 color CMOS camera. A 2 $Kmin^{-1}$ rate was used for both cooling and heating. Elemental analyses of C, H, and N were performed by means of a Perkin–Elmer 2400 series II device, after combustion at 850 °C, using IR detection and gravimetry. Thermogravimetric analysis and differential scanning calorimetry data were acquired simultaneously using a METTLER DSC3+ analyser under a 50 $mL.min^{-1}$ air flow at 10 $K.min^{-1}$ heating rate. Magnetic susceptibility data were collected with a Quantum Design MPMS-XL SQUID magnetometer at heating and cooling rates of 2 $Kmin^{-1}$ in a magnetic field

of 1 kOe.Thermomechanical testing was performed on a temperature-controlled tensile stage (Linkam Scientific, TST-350). To perform constant strain testing, the temperature is first set to 30 or 45 °C where the sample is equilibrated pendant 15 minutes. Then, we set an initial stress by increasing the clamp-clamp distance by 12 micrometers. The probe is equilibrated during 15 minutes more. Once equilibrium is achieved (no fluctuations in the registered force) the temperature cycling begins. Simultaneously, a series of photos, focused on the fracture zone, are acquired at a rate of one photo per °C, which allow us to track the color change associated with the spin transition. After the first temperature cycling, the sample is equilibrated before the distance between the clamps is increased again by 12 micrometers, followed by a second temperature cycle. This procedure is repeated 5 times for each sample.

Figure S1. Spin crossover properties of the $[Fe(NH_2trz)_3]SO_4$ complex and SCO composite.

Thermal variation of χT for the microcrystalline powder sample (top panel) and for the composite (bottom panel) for two heating-cooling cycles. The second thermal cycle leads systematically to a smaller hysteresis width, which becomes stable for further cycling. This "run-in effect" is typical for many SCO compounds and may be related to the loss of residual solvent molecules. The insert shows a TEM image of the rod-shaped microparticles.

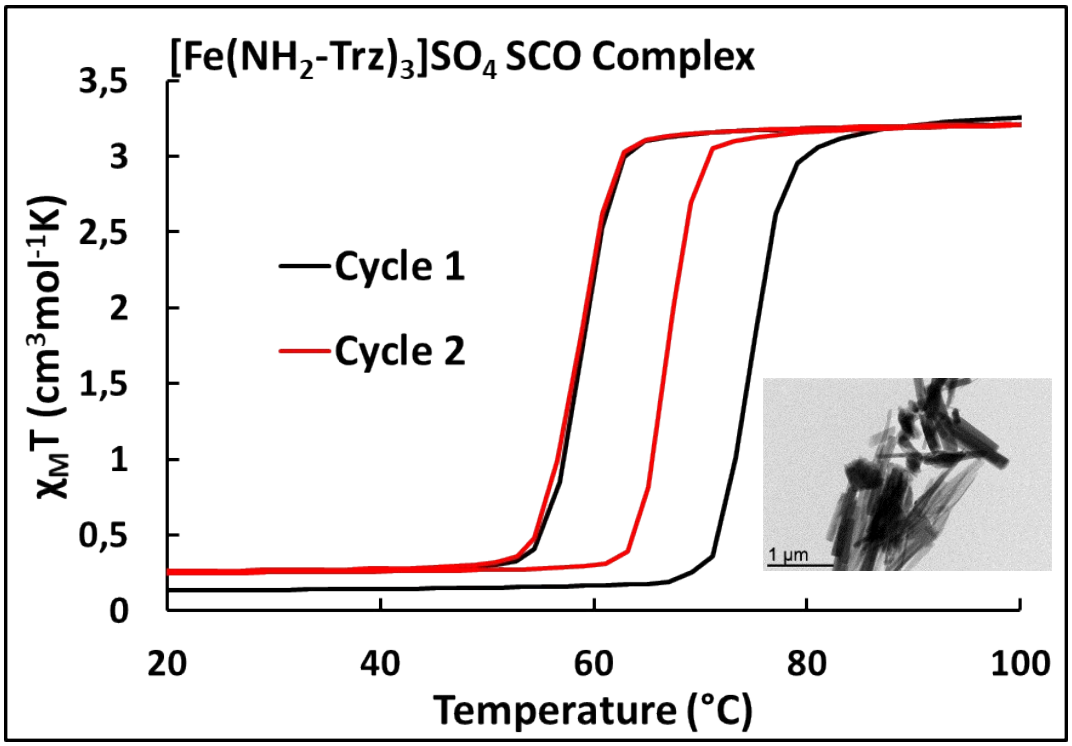

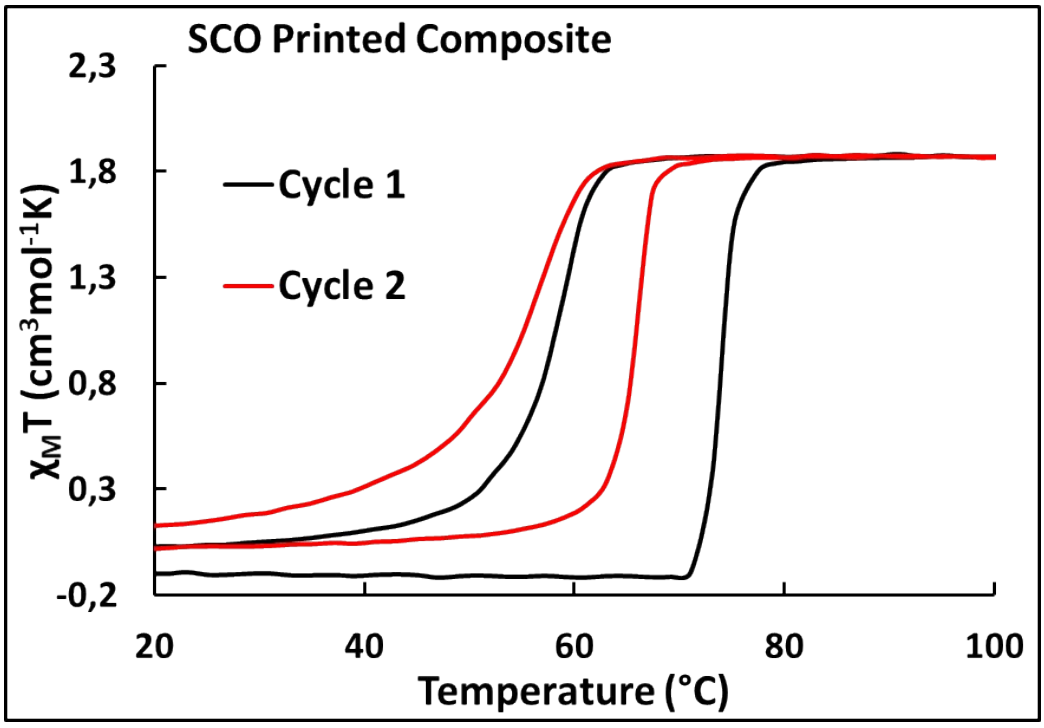

Figure S2: Photos of the 4D printed bimorph structure (a) for 20 wt% SCO load and (b) for an underexposure near the interface between the two layers. For loads above ca. 15wt% the sample becomes brittle, whereas an inappropriate curing results in delamination.

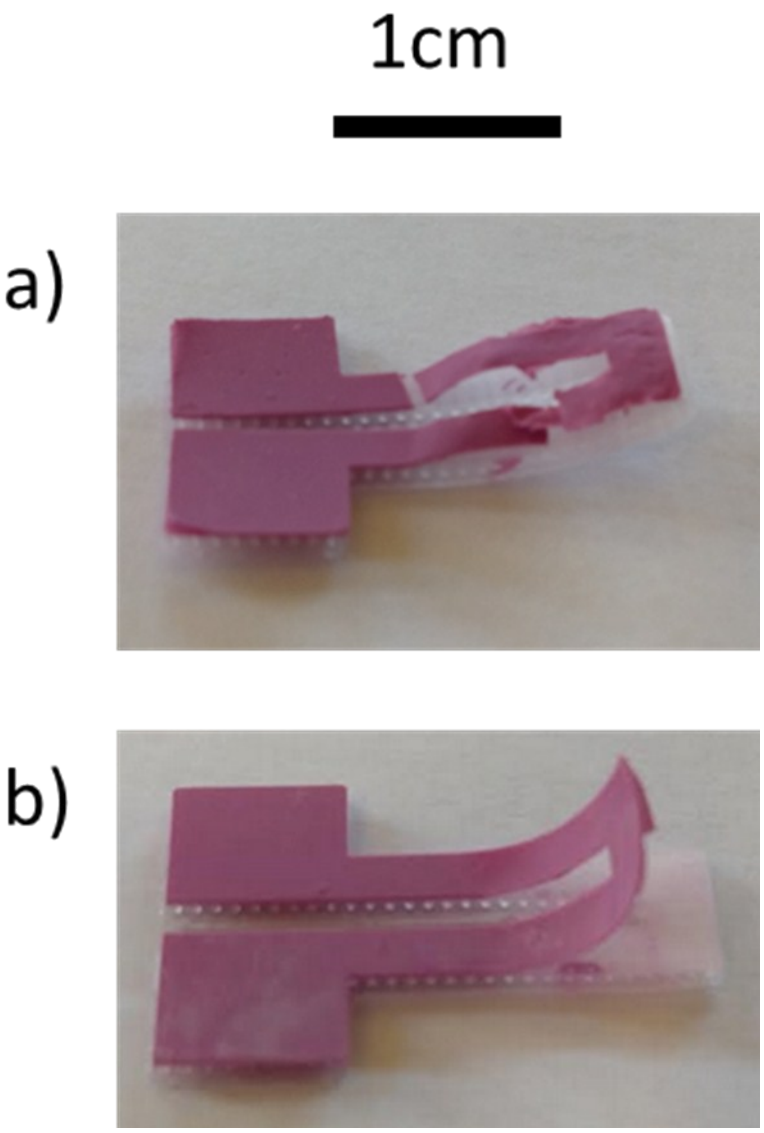

Figure S3: DSC and TG analysis of the DS-3000 polymer, SCO complex and the SCO-polymer composite

DSC and TG analysis of the DS3000 polymer

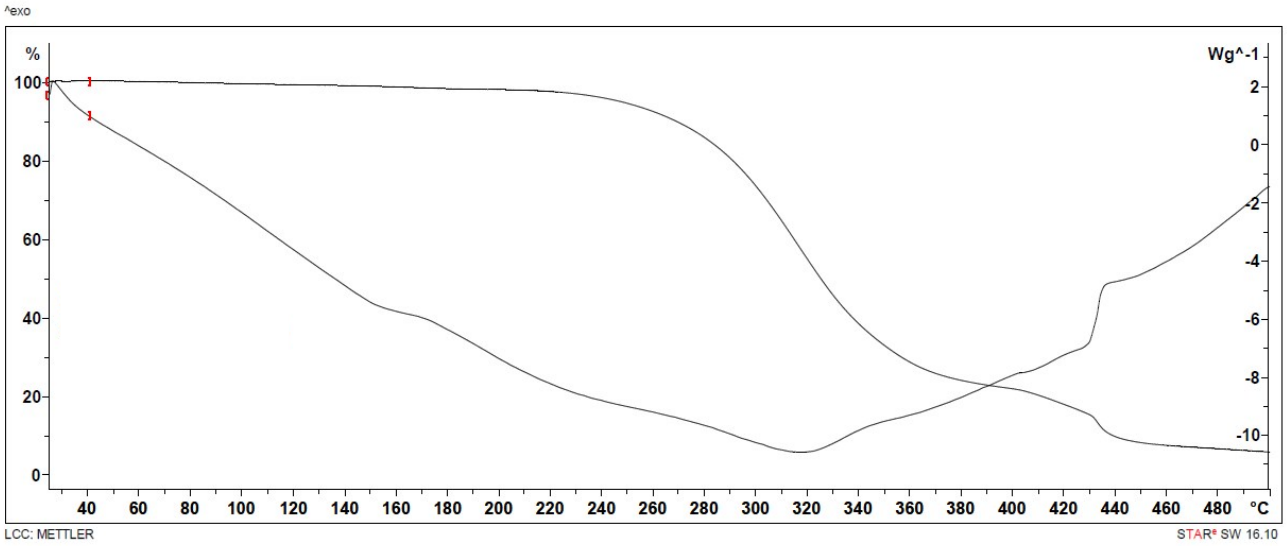

DSC and TG analysis of the SCO complex

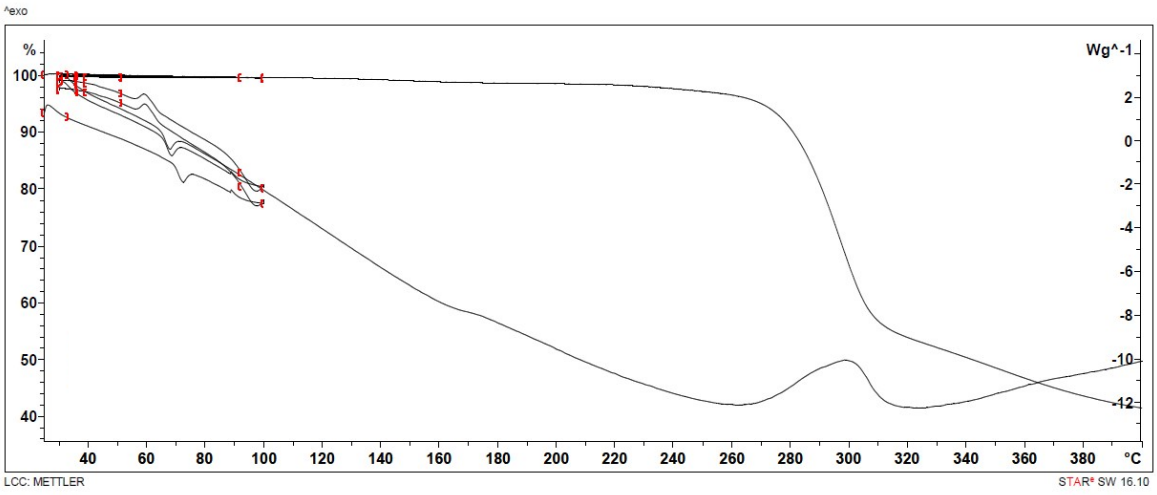

DSC and TG analysis of the SCO-polymer composite

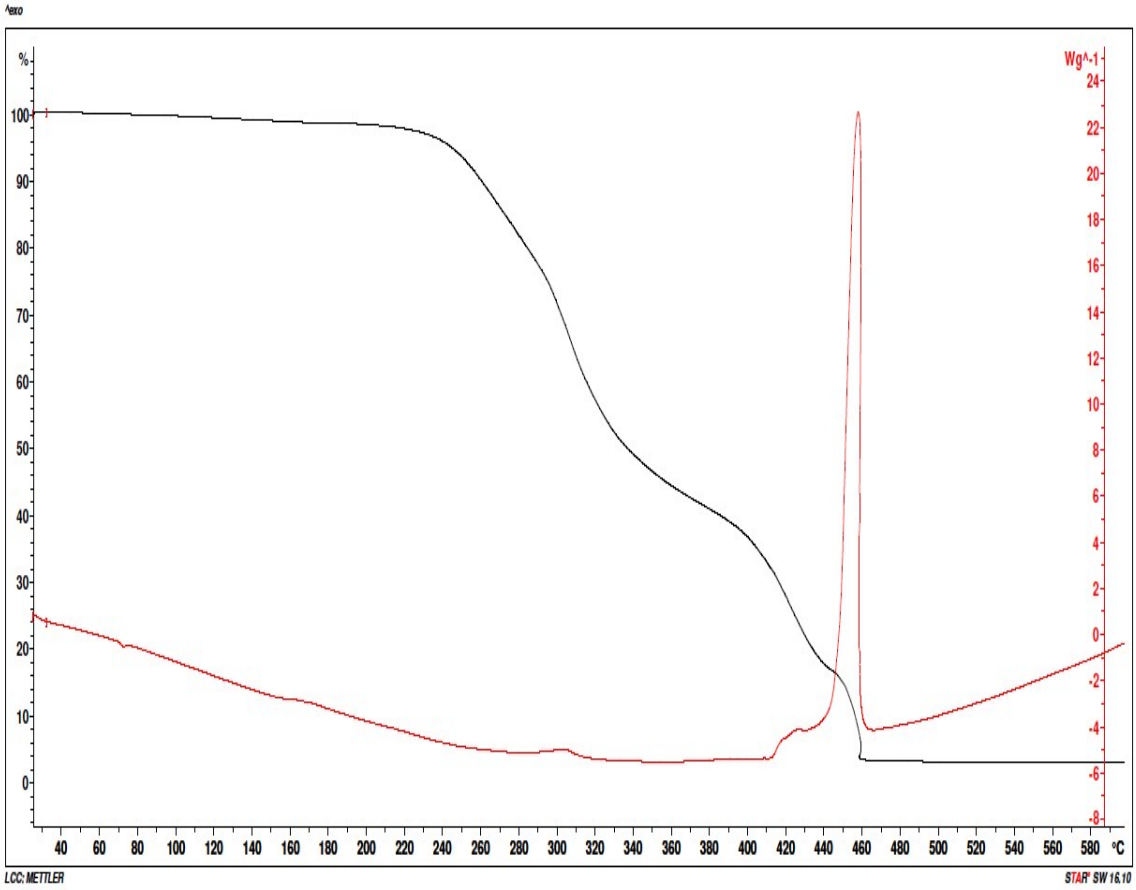

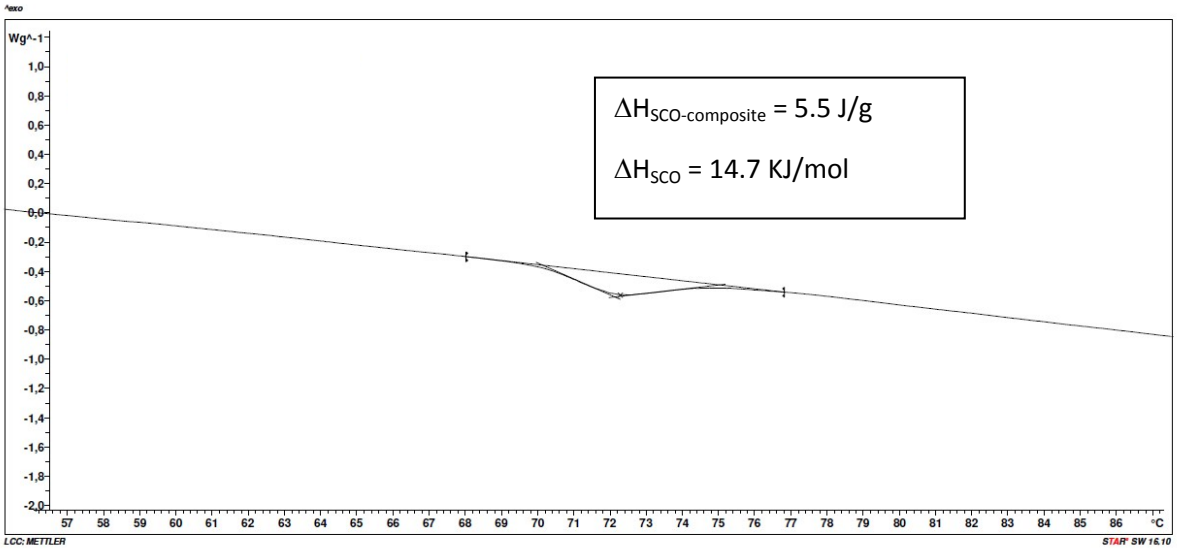

$\Delta H_{SCO\text{-}composite}$ = 5.5 J/g

ΔH_{SCO} = 14.7 KJ/mol

Figure S4. SEM image and EDX analyses corresponding to the selected area of the two layers of the bimorph architecture. (A Pt layer was deposited on the sample for the SEM observation.)

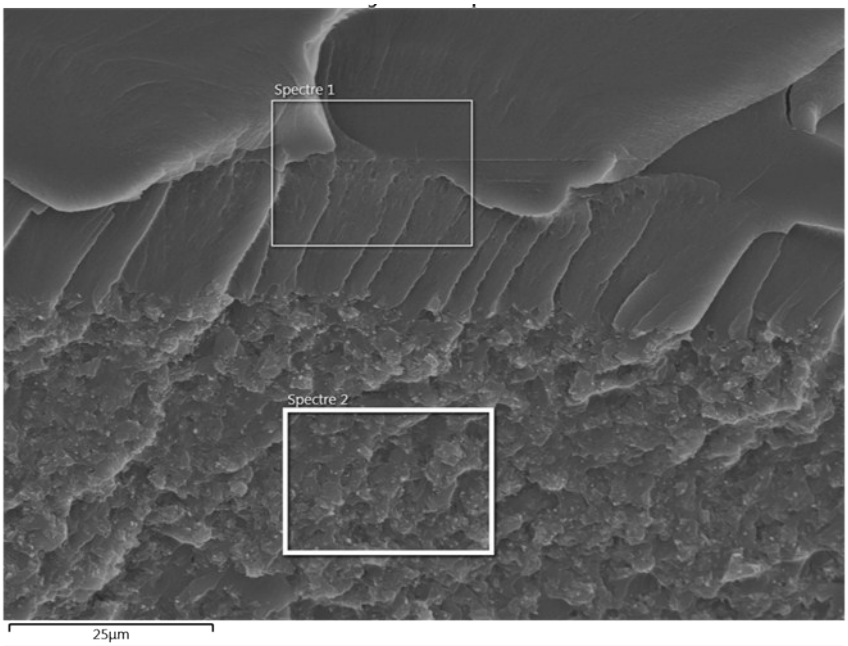

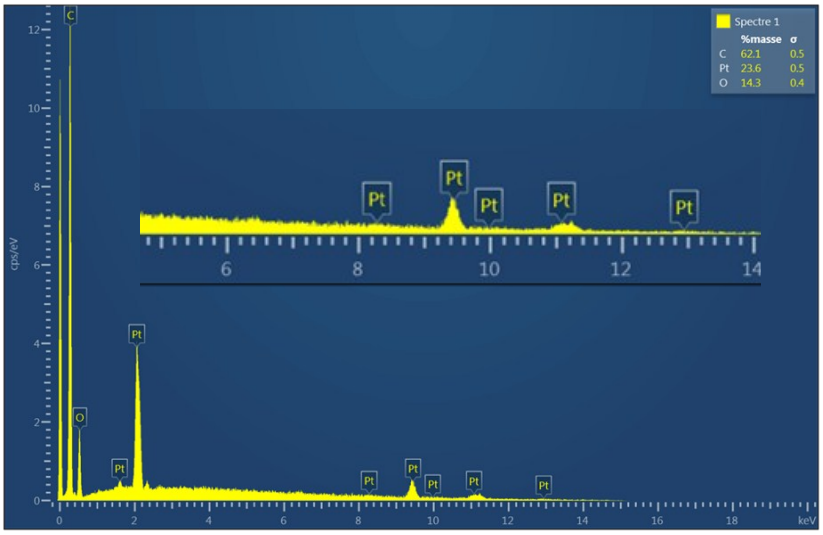

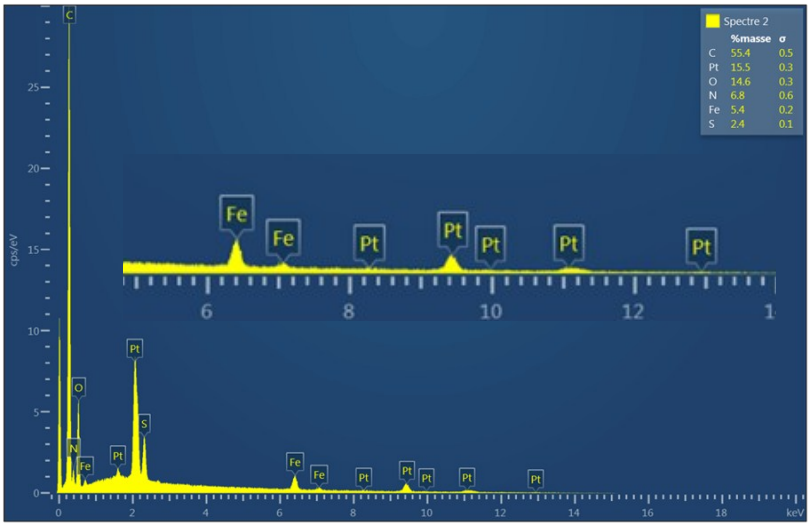

Figure S5. Colour change upon the SCO, associated bending of bimorph actuators and corresponding actuation cycle upon heating and cooling for (a) 150 µm active layer and 90 µm inactive layer and (b) 850 µm active layer and 150 µm inactive layer.

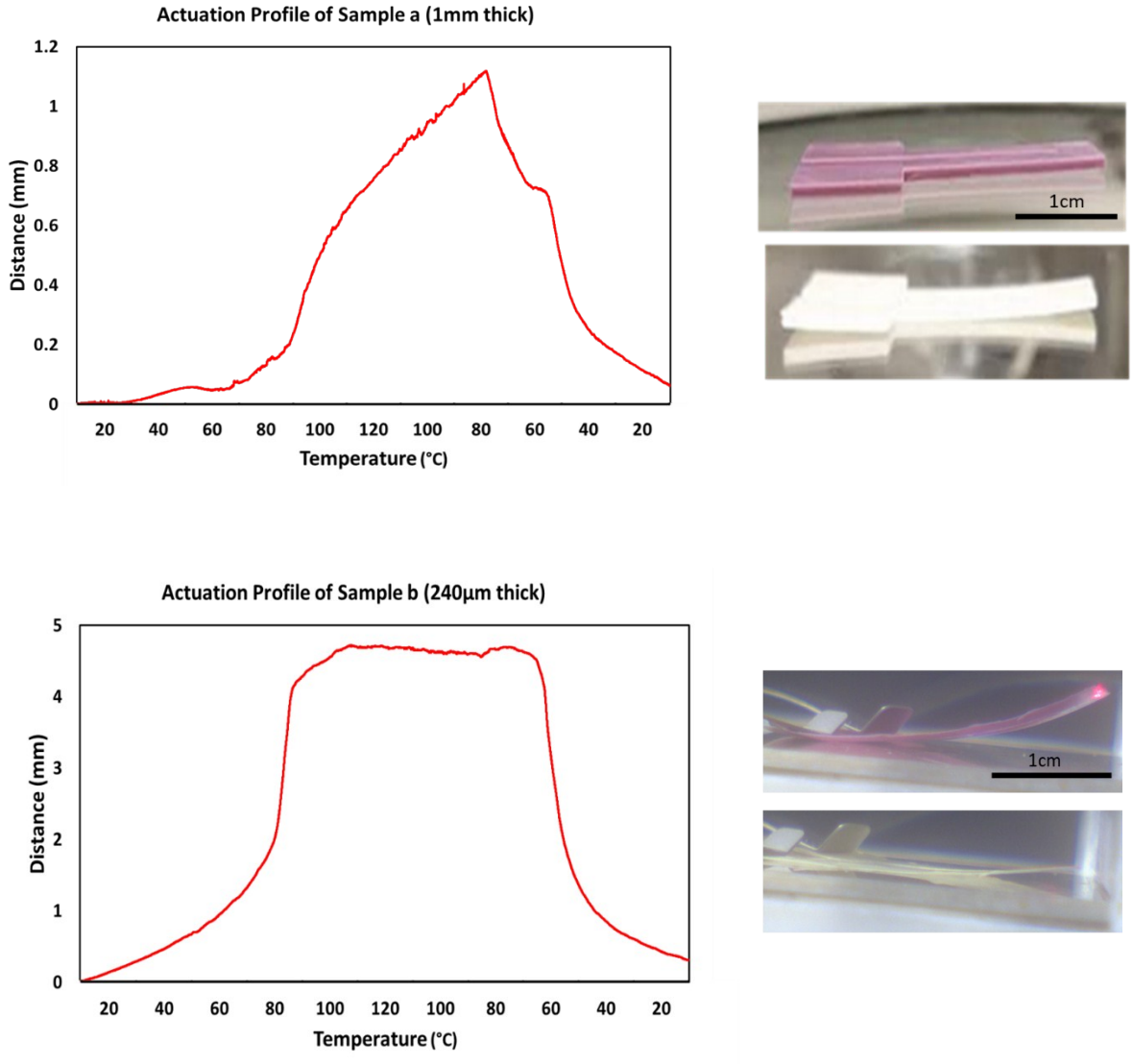

Actuation properties of the 3D printed composite

A rectangular bilayer strip with dimensions 2 cm x 0.4 cm x 240 µm was 3D printed to perform a controlled temperature cycle and extract the actuation properties of the material using the Timoshenko beam theory.[19]

Figure S6. Movement of a rectangular printed strip upon the spin transition.

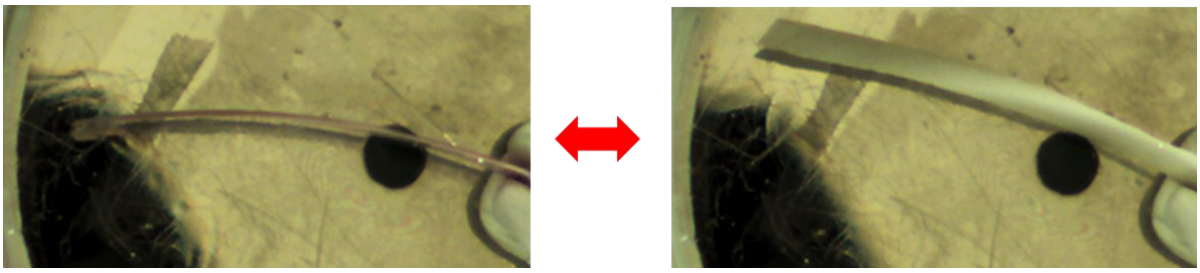

Using Timoshenko's beam theory, as it has been discussed before[12], it is possible to associate the change in curvature k of a bilayer beam to the strain produced by the spin transition $\Delta L/L$:

$$k = \frac{6(\alpha_2 \Delta T + \frac{\Delta L}{L} - \alpha_1 \Delta T)(1 + m^2)}{h[3(1 + m^2) + (1 + mn)\left(m^2 + \frac{1}{mn}\right)]} \quad (1)$$

with

$$m = \frac{a_1}{a_2} \quad (2)$$

$$n = \frac{E_1}{E_2} \quad (3)$$

$$h = a_1 + a_2 \quad (4)$$

where a_i is the thickness, E_i is the Young's modulus and α_i is the thermal expansion coefficient of each layer. ΔT is the temperature range of interest. In this case, the temperature range is restricted to exactly that of the SCO to isolate the effect of the spin transition from the effect of thermal expansion coefficient mismatch between the two layers. The parameters a_1 and a_2 were 0.09 mm and 0.15 mm respectively. The Young's moduli of each layer at the SCO temperature were obtained from thermomechanical analysis as: $E_1 = 280$ MPa and $E_2 = 190$ MPa. The linear thermal expansion coefficients were likewise obtained from temperature-controlled mechanical testing as: $\alpha_1 = 6.5 \cdot 10^{-4}$ K^{-1}, $\alpha_2 = 9 \cdot 10^{-4}$ K^{-1}. The change in curvature can be estimated from the tip deflection δ for relatively small deflections by the following relationship:

$$\delta = \frac{kL^2}{2} \quad (5)$$

It should be noted however that there is a significant uncertainty in the measurement of the tip deflection δ, caused by the fact that the bilayer strip bends slightly to the side as it performs its movement.

With these parameters, the strain of the active layer caused by the spin transition is estimated as: ΔL/L = 0.0033. We can then calculate the volumetric work density W/V of the actuator:

$$\frac{W}{V} = \frac{E(\frac{\Delta L}{L})^2}{2} \quad (6)$$

giving W/V = 1.5 mJ·cm^{-3}.

Table S1. Comparison of Young's modulus, strain and work density of selected polymer-based bending actuators.

Active material	Actuator dimension (mm)	Young's modulus (GPa)	Strain (%)	Work density (mJ/cm^3)	Ref.
Nylon	90 × 3 × 0.87	0.4	2.5	125	S1
PEDOT	6 × 1 × 0.018	0.00033	0.5	0.004	S2
Bucky gel	8 × 4 × 0.465	0.26	1.9	45	S3
Polypyrrole	0.58 × 0.22 × 0.16	0.12	14	1180	S4
Ru-solfoxide polymer	5 × 1 × 0.002	0.02	0.105	0.0055	S5
SCO-SU8	0.84 × 0.1 × 0.0235	3.2	1	140	S6
SCO-DS3000	20 × 4 × 0.24	0.28	0.33	1.5	Present work

References:

S1 S. M. Mirvakili, I. W. Hunter, Adv. Mater. 2017, 29, 1604734.

S2 T. N. Nguyen, K. Rohtlaid, C. Plesse, G. T. M. Nguyen, C. Soyer, S. Grondel, E. Cattan, J. D. W. Madden, F. Vidal, Electrochim. Acta 2018, 265, 670.

S3 K. Mukai, K. Asaka, K. Kiyohara, T. Sugino, I. Takeuchi, T. Fukushima, T. Aida, Electrochim. Acta 2008, 53, 5555.

S4 G. Alici, V. Devaud, P. Renaud, G. Spinks, J. Micromech. Microeng. 2009, 19, 025017.

S5 Y. Jin, S. I. M. Paris, J. J. Rack, Adv. Mater. 2011, 23, 4312.

S6 M. D. Manrique-Juárez, F. Mathieu, A. Laborde, S. Rat, V. Shalabaeva, P. Demont, O. Thomas, L. Salmon, T. Leichle, L. Nicu, G. Molnár, A. Bousseksou, Adv. Func. Mat., 2018, 1801970.